# Experimental and numerical analysis of injection-induced permeability changes in pre-existing fractures

Ouf, Josselin; Osten, Julian; Luo, Wen; Khaledi, Kavan; Jalali, Mohammadreza; Vardon, Philip J.; Amann, Florian

**DOI**
10.1016/j.gete.2024.100576

**Publication date**
2024

**Document Version**
Final published version

**Published in**
Geomechanics for Energy and the Environment

**Citation (APA)**
Ouf, J., Osten, J., Luo, W., Khaledi, K., Jalali, M., Vardon, P. J., & Amann, F. (2024). Experimental and numerical analysis of injection-induced permeability changes in pre-existing fractures. *Geomechanics for Energy and the Environment*, *39*, Article 100576. https://doi.org/10.1016/j.gete.2024.100576

Geomechanics for Energy and the Environment 39 (2024) 100576

Contents lists available at ScienceDirect

Geomechanics for Energy and the Environment

journal homepage: www.elsevier.com/locate/gete

# Experimental and numerical analysis of injection-induced permeability changes in pre-existing fractures

Josselin Ouf [a,c,*], Julian Osten [a], Wen Luo [a,c], Kavan Khaledi [b], Mohammadreza Jalali [a], Philip J. Vardon [c], Florian Amann [a,b]

[a] Department of Engineering Geology and Hydrogeology, RWTH Aachen University, Aachen, Germany
[b] Fraunhofer Institute for Energy Infrastructure and Geothermics, IEG, Aachen, Germany
[c] Geo-Engineering Section - Delft University of Technology - Delft, The Netherlands

ARTICLE INFO

Editors-in-Chief:
Professor Lyesse Laloui and Professor Tomasz Hueckel

*Keywords:*
Hydraulic stimulation
Enhanced Geothermal Systems
Permeability enhancement
Fault reactivation
Hydro-mechanical modeling
Granite

ABSTRACT

This paper presents a combined laboratory and numerical investigation on the injection-induced permeability changes in pre-existing fractures. The analyses conducted were primarily based on the results of an innovative laboratory experiment designed to replicate the key mechanisms that occur during hydraulic stimulation of naturally fractured rocks and/or faulted zones. The experiment involved pressure-controlled fluid injection into a laboratory-scale pre-existing fracture within a granite block, which was subjected to true triaxial stress conditions. Rough and smooth fractures are investigated, and the results are discussed. Based on the experimental results, two contributing mechanisms were considered to describe the pressure-driven permeability changes in pre-existing fractures: (1) elastic opening/closure leading to a reversible permeability change, and (2) fracture sliding in shear mode, causing dilation and hence an irreversible permeability increase. With these assumptions, an aperture-dependent permeability function was adopted to couple the hydraulic flow with the mechanical deformations along the fracture. Subsequently, a 3D coupled hydro-mechanical model was developed to replicate fluid-injection tests conducted at various conditions, including different stress conditions and fracture surface roughness. The employed modeling framework effectively captured the experimental observations. Our results indicate that the maximum permeability increases twofold.

## 1. Introduction

### 1.1. Background

The utilization of geothermal energy for electricity generation is considered to be technically and economically viable at temperatures above 120 °C.[1]To reach such temperatures, in most locations deep wells must be drilled to depths of 3 to 5 km,[2] depending on the local geothermal gradient and the presence of permeable zones at the targeted site, which are usually found in the form of naturally fractured rocks and/or faulted zones. Therefore, fractured zones play an important role in deep geothermal systems as they are the main conduits for fluid flow and heat transfer. However, unlike shallow hydrothermal systems in porous formations, deep geothermal resources are typically characterized by hot-dry conditions and exhibit low permeability values (less than $10^{-16}$ $m^2$,[3,4]) which present challenges for water circulation and heat extraction from these resources. An engineering solution to artificially enhance the permeability in deep formations is the so-called hydraulic stimulation technique, which involves injecting high-pressure fluid, usually water or brine, into a low-permeability rock mass in order to reactivate pre-existing fractures in shear mode (HS: hydro-shearing) or potentially creating new fractures in tensile mode (HF: hydro-fracturing).[5] However, high-pressure fluid injection into a geothermal reservoir inevitably induces micro-seismic events around the injection zone, primarily due to the reactivation of critically stressed fractures in shear mode.

From an engineering perspective, two competing, but inter-connected, objectives should be targeted in any hydraulic stimulation practice, i.e. (1) significantly increasing the permeability of the reservoir to an economically viable level, and (2) simultaneously controlling the induced seismicity below a hazardous level.[6] HS has been successfully implemented in numerous Enhanced Geothermal Systems (EGS), often resulting in a permeability increase of up to 2–3 orders of magnitude. Notable examples include Soultz-sous-Forets in France,[7,8] Cooper Basin in Australia,[9] Fenton Hill in New Mexico, USA.[10,11] Although a significant portion of seismic events that occur during hydraulic

* Corresponding author at: Department of Engineering Geology and Hydrogeology, RWTH Aachen University, Aachen, Germany.
*E-mail address:* ouf@lih.rwth-aachen.de (J. Ouf).

https://doi.org/10.1016/j.gete.2024.100576
Received 23 February 2024; Received in revised form 13 June 2024; Accepted 12 July 2024
Available online 20 July 2024

stimulation are below the sensitivity level, it is possible that reservoir stimulation may result in induced seismicity above a hazardous threshold. Such seismic events have been unfortunately experienced in the past in a limited number of EGS projects, as demonstrated by incidents in Pohang in Korea,[12] Basel in Switzerland[13] and Vendenheim near Strasbourg in France[14] which raised public concerns. Nonetheless, the sustainability of permeability enhancement over time may be uncertain. For example, in the hydraulic stimulation test conducted as part of the St1 Deep Heat Project in southern Finland, permeability initially increased by two orders of magnitude but gradually returned to its natural value after pressure recovery.[15] These examples highlight the complexity of hydraulic stimulation outcomes and the factors influencing the permeability enhancement.

### 1.2. State-of-the-art in hydraulic stimulation

To effectively increase the permeability of a geothermal reservoir through hydraulic stimulation while mitigating the induced seismicity, it is important to have a comprehensive understanding of various influencing factors,[16] including the site characteristics (in-situ stress state, pore pressure, temperature), fault/fracture properties (type, dip, dip direction, frictional strength, permeability, etc.), host rock properties (stiffness, UCS, tensile strength, permeability, heat conductivity, etc.) and the injection data (the injection type, duration, location, etc.). Numerous field investigations have been conducted over the past decades to explore the underlying processes that occur during reservoir stimulation at different spatial and temporal scales (e.g. see[17] for a comprehensive review). Among them, the hydraulic stimulation experiments on fractured granite at Grimsel Test Site (GTS)[5,6] and the fault-reactivation experiment in clay shale at Mont-Terri Underground Rock Laboratory (MT-URL)[18–20] are worth mentioning. These field experiments have provided valuable insights into the risks, limitations, and technical challenges associated with hydraulic stimulation in real-size geothermal systems.

The roughness of fractures significantly affects their hydromechanical behavior. Barton et al.[21] demonstrated that fractures with varying Joint Roughness Coefficients (JRCs) exhibit differences tangential stiffness, normal stiffness, friction angle, cohesion and dilation angle when subjected to different shear and normal loads. Tsang et al.[22] findings indicate that under normal loading, fracture roughness impacts the initial aperture and the variation of normal aperture, consequently affecting the flow rate, which tends to be higher in rough fractures. Moreover, differences in fracture roughness give rise to varying contact areas. Consequently, the stress exerted in the contact region exceeds predictions solely based on dividing the total load by the total fracture area. The presence of shear stress can induce damage to the fracture surface, altering the asperity geometry through processes such as abrasion, smoothing, or roughness enhancement. The extent of these changes depends on the initial fracture roughness and the applied load.[23,24]

In addition to field investigations, numerous laboratory-scale experiments have been designed over the past decades with the aim of down-scaling the fluid injection process in geothermal reservoirs (see e.g.[25–28]). These small-scale laboratory experiments provide the means to constrain various field-related parameters that can naturally be subjected to uncertainties. This allows for the investigation of fundamental hydro-mechanical processes occurring during both reservoir stimulation and geothermal operation under pre-defined/controlled conditions. An essential aspect in this context which has been investigated experimentally, is the changes in fracture permeability resulting from fluid injection. Numerous experimental studies have indicated that fracture permeability tends to increase as the effective normal stress applied to the fracture decreases as a result of increases in fluid pressure (e.g. see[29–31]). Dilation triggered by shearing has been identified as the primary mechanism responsible for the irreversible increase in hydraulic aperture, and consequently a sustainable enhancement in the fracture permeability.[32]

Another crucial aspect in the context of geothermal reservoir engineering, which has been the subject of intensive research in recent years, is the development of reliable numerical models capable of reproducing the coupled hydro-mechanical processes in deep geothermal systems. In general, the numerical approaches introduced to describe the coupled multi-physics processes in geothermal reservoirs can be categorized into two groups[33]: (1) continuum-based models and (2) discontinuum models. In continnum-based models, the fractured zones and faults are considered as a porous media with equivalent thermo-hydro-mechanical properties. This modeling approach has been widely employed in geothermal reservoir modeling to describe injection-induced fault reactivation,[20,34,35] induced seismicity,[36,37] as well as the temporal and spatial development of temperature and fluid pressure.[38,39] In contrast, discontinuum models rely on the explicit representation of fractures in the rock matrix. The most common discontinuum modeling techniques include (1) FEM-DEM/cohesive zone modeling,[40,41] (2) Discrete Fracture Network using interface element,[42] (3) embedded lower dimensional element.[43] While continuum-based models offer a simplified representation of fractured zones and faults by treating them as porous media, discontinuum models take a more explicit approach by directly representing fractures within the rock matrix. Both modeling strategies have their strengths and limitations, and the choice between them depends on the specific geothermal reservoir characteristics and the phenomena under investigation.

### 1.3. Objectives

There is a scarcity in the literature regarding numerical modeling and experimental set-up that accurately replicates smaller-scale HS, where experimental conditions are well-characterized and experimental results are closely monitored[6,44]. Most laboratory experiments conducted so far have been conducted in triaxial apparatus, leading to limited stress control. Additionally, the predominant use of cylindrical samples with restricted dimensions has resulted in boundary conditions close to the injection point and limited representativeness of fracture surfaces. To address these limitations, our study introduces a novel approach. We employ a unique true triaxial machine coupled with injection into an artificial fault at a decimeter scale. This setup offers a controlled environment for exploring the hydromechanical behavior of pre-existing fractures. The true triaxial machine allows for precise stress control, ensuring that experimental conditions can better replicate real-world scenarios. Secondly, injecting fluids into an artificial fault at a decimeter scale provides a fracture surface that is more representative than cylindrical samples, which are often limited in length.

In contrast to previous methods where fracture behavior modeling, such as with TOUGH-FLAC, utilized a staggered coupling approach resulting in a partially coupled solution, the numerical approach employed here within the MOOSE framework is fully coupled.

The focus in this study lies on the mechanisms that lead to permeability enhancement in pre-existing fractures as a result of pressurized fluid injection. During reservoir stimulation, fluid injection increases fluid pressure and reduces the effective normal stress on pre-existing fractures. This may trigger sliding along critically stressed fractures, resulting in irreversible fracture opening (dilation) and, consequently, an increase in their permeability. Carefully down-scaled laboratory and modeling analyses can be useful to illuminate the relationship between permeability and mechanical characteristics in pre-existing fractures, as illustrated in Fig. 1. With this motivation, this study aimed to achieve the following objectives:

- To design and carry out a laboratory-scale testing procedure to gain a deeper understanding of permeability change during the hydraulic stimulation of pre-existing fractures in a range of conditions. The experiments are designed to replicate the mechanisms influencing the evolution of flow rates due to pressurized water injection within a fracture. The experiments are conducted using

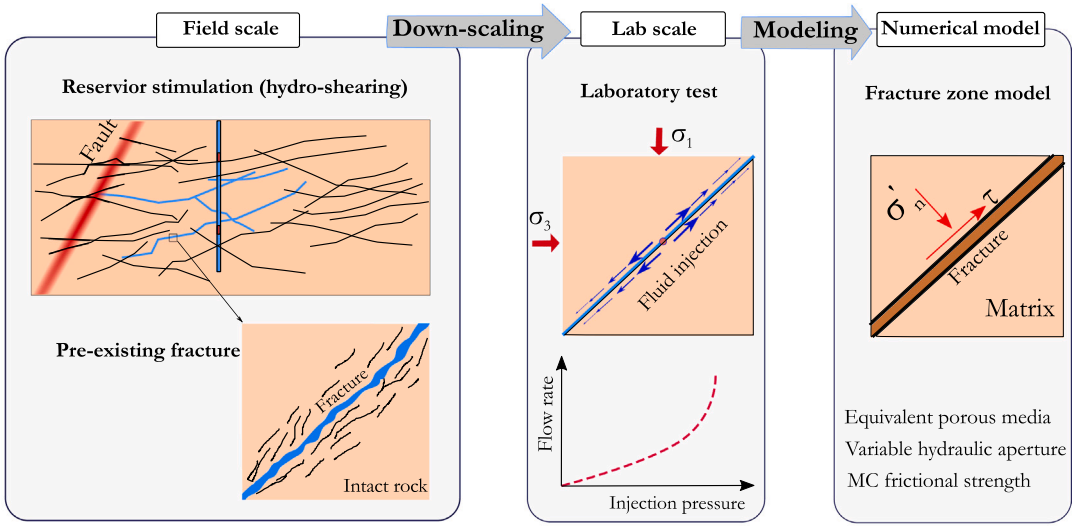


**Fig. 1.** Figure showing the overall objectives of this study including (1) design and perform laboratory experiments that scale down the hydro-shearing process, (2) develop numerical models capable of reproducing the injection-induced permeability change in pre-existing fractures.

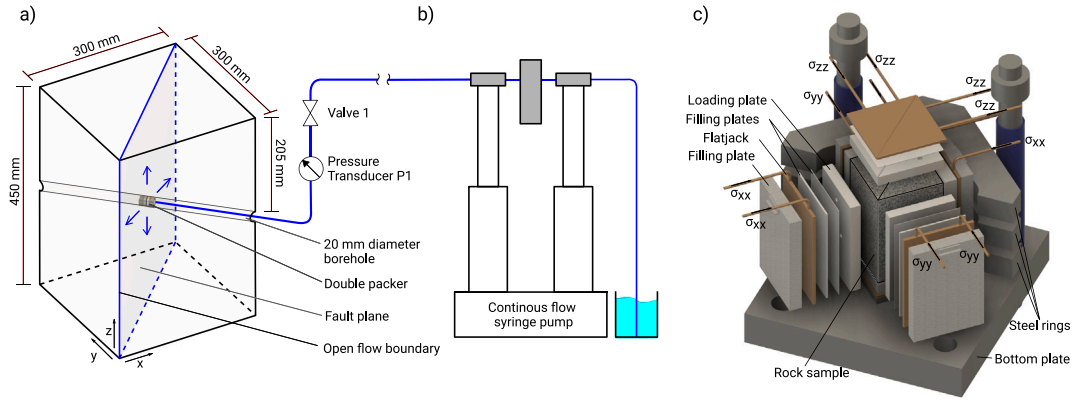


**Fig. 2.** A schematic representation of triaxial testing setup for hydro-shearing; (a) a granite block with a vertical fault plane is shown. The fluid is injected through a borehole with a diameter of 20 mm. Water can flow out at the fault boundaries. The injection interval is isolated by a double packer system; (b) the injection unit consisting of a flow pump and a pressure transducer; (c) the true triaxial loading apparatus.

a true triaxial machine which controls the three principal stress components on an artificial fault at a decimeter scale. Different fracture roughnesses and their influence on the permeability are investigated.

- To develop and validate a suitable modeling framework to describe the hydro-mechanical processes resulting from high-pressure fluid injection in pre-existing fractures. The developed model provides a numerical description for the injection-induced permeability changes. The numerical modeling used is fully coupled and solved without staggering.

## 2. Methodology

### 2.1. Methodology for the laboratory experiments

A series of fluid-injection tests into pre-existing fractures were conducted at room temperature (20 °C) using a True Triaxial Rock Testing Machine. The testing apparatus was originally developed to investigate fracture initiation and propagation in intact rock during hydraulic fracturing experiments[45] and these data were used to calibrate and validate numerical modeling.[26,46] The setup and sample configuration were modified for the purpose of the experiments presented in this study.

#### 2.1.1. Sample preparation and experimental apparatus

The rock used in the experiments was an isotropic, fine-grained and low-permeability granite (Tittinger Feinkorn) cored from the Höhenberg quarry in Bavaria, Germany. It was composed of 45% quartz, 25% potassium feldspar, 20% plagioclase, and 7.5% biotite.[47] The samples were cuboid-shaped, saw cut, and polished to a size of 300 mm × 300 mm × 450 mm with a precision of ±0.05 mm and parallelity of ±0.001 mm. A discontinuity/fracture (laboratory-scale fault) was then created by saw cutting the cuboid into two prisms along the diagonal of the sample (Fig. 2). The resulting surfaces were further ground and polished. Two roughness values were chosen for the fracture plane in the tests: (1) a smooth fracture surface polished with 1200 grit silicon carbide (SiC) powder and (2) the rough surface fracture polished with 40 grit SiC powder. The samples also contained a borehole with a diameter of 20 mm, crossing the fracture plane perpendicularly (Fig. 2). A double packer system was employed to establish a 2 mm-long isolated interval along the borehole, containing the fracture. During the experiments, the de-ionized water was injected at room temperature by a dual-pump setup of two ISCO 500D syringe pumps allowing continuous flow of up to 200 ml/min. The fluid was transferred by a steel capillary with a diameter of 2 mm into the isolated interval. The two packers were not connected allowing free kinematic movement along the isolated interval. The injection pressure was measured by

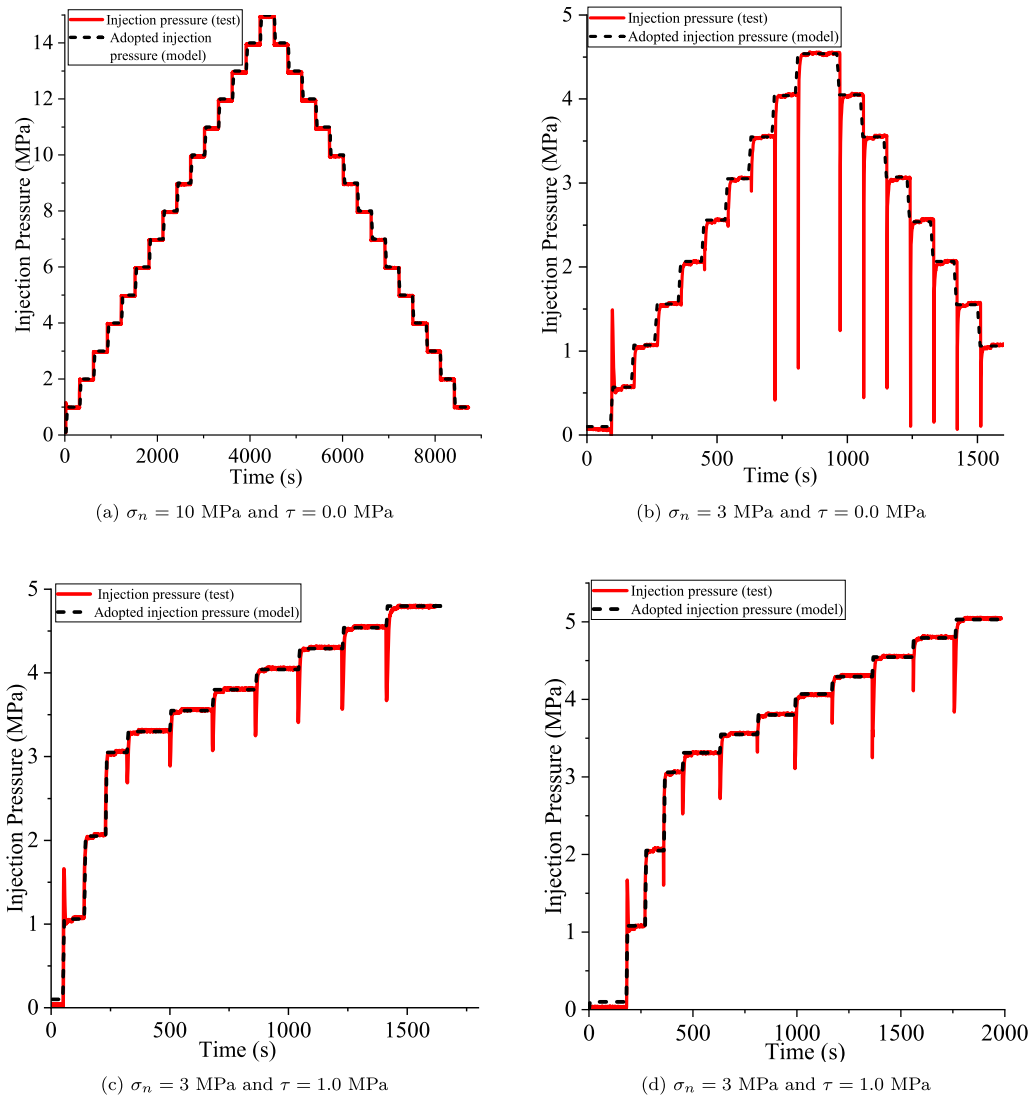


**Fig. 3.** Injection protocols for the conducted hydraulic stimulation tests along with the adopted injection pressure in the numerical simulations; (a) Test 1, isotropic loading/smooth fracture; (b) Test 2, isotropic loading/rough fracture; (c) Test 3, shear loading/rough fracture; (d) Test 4, shear loading/rough fracture.

a Keller 300× pressure transducer outside the sample and flow was controlled by a valve between the packer and the pump (Fig. 2).

The granite block was confined by three sets of oil-filled flatjacks, which were independently controlled by a system of three Automatic Pressure Controller syringe pumps (Wille VPC). The horizontal stresses were both applied by two opposing, rectangular flat jacks ($\sigma_{xx}$ and $\sigma_{yy}$ in Fig. 2). The vertical stress ($\sigma_{zz}$) was induced by two sets of opposing, triangular flatjacks that retrace the fault. The stresses were transferred to the granite block by steel load plates, covered with teflon foil to reduce friction between metal and rock. The loading unit was held in place by several filling plates and three steel rings at the side and two steel plates at the top and bottom. The fracture was drained to all sides. All corners of the rock blocks were open to the atmosphere and bevelled edges of the fracture allowed discharge to the top and bottom between the sample and load plates.

### 2.1.2. Testing procedures and injection protocols

The following hydraulic tests were conducted considering different settings in terms of the applied stress conditions and fracture surface roughness:

- Test 1 (isotropic loading/smooth fracture): in the first test, a granite block with a smooth fracture plane was isotropically loaded at the constant stress of $\sigma_{xx} = \sigma_{yy} = \sigma_{zz}$= 10 MPa. The initial normal stress applied on the fracture plane was then $\sigma_n$ = 10 MPa. The fluid injection process involved step-wise increasing the water pressure in the isolated interval by 1 MPa every 300 s until it reached almost 15 MPa. Subsequently, the pressure recovery was performed by gradually decreasing the pressure by 1 MPa every 300 s until it returned to 1 MPa (Fig. 3(a)).
- Test 2 (isotropic loading/rough fracture): in the second test, the injection test was performed on a sample with a rough fracture plane. The sample was isotropically confined at the stress of $\sigma_{xx} = \sigma_{yy} = \sigma_{zz}$= 3 MPa. Accordingly, the initial normal stress applied on the fracture plane was $\sigma_n$ = 3 MPa. The water injection process consisted of step-wise increment of water pressure by 0.5 MPa every 80 s until it reaches 4.5 MPa, followed by a gradual decrease of 0.5 MPa every 80 s until it returns to almost 1 MPa (Fig. 3(b)).
- Tests 3 and 4 (shear loading/rough fracture): two tests were performed on a sample with a rough fracture plane subjected to a pre-defined shear stress. The applied stresses to the granite block in these tests were $\sigma_{xx}$ = 4 MPa, $\sigma_{yy}$ = 2 MPa, and $\sigma_{zz}$ = 3 MPa, theoretically resulting in a mean stress of $\sigma_n = (\sigma_{max} + \sigma_{min})/2$ = 3 MPa, and the shear stress of $\tau = (\sigma_{max} - \sigma_{min})/2$ = 1 MPa. The injection process involves gradually increasing the water pressure

until it reaches almost 5 MPa (Figs. 3(c) and 3(d)). When further increasing the injection pressure, the flow rate rose sharply until it reached the upper limit of the injection pump, which was then shut off. Accompanied by a distinct stress drop, this prevented the accomplishment of a step-down phase as seen in tests 1 and 2.

All tests were planned with a normal stress of 10 MPa, but when the rough sample was tested, the fracture was too permeable to reach injection pressures in the range of 10 MPa within the capacity of the injection pump.

### 2.2. Methodology for the coupled HM-modeling

An Equivalent Continuum Modeling approach (ECM) was employed to describe the hydro-mechanical processes in pre-existing fractures. To accomplish this, the fracture was modeled as a finite-thickness porous medium with equivalent hydro-mechanical properties. The intact rock was considered as a low-permeable material. An aperture-dependent permeability function was adopted to describe the permeability changes of the fracture zone. The fracture permeability model was implemented by the authors in the multi-physics finite element code MOOSE framework.[48] We also employed the PorousFlow and TensorMechanics module to solve the coupled hydro-mechanical equations.[49] The coupled equations to be solved in both the fracture zone and the intact rock include: (1) the momentum balance equation, and (2) the mass balance of the liquid phase. The following subsections provide more details on the theoretical and modeling assumptions employed in this study.

#### 2.2.1. Mechanical formulations

The following equation holds across the entire domain (intact rock and fracture) to satisfy the balance of linear momentum (the gravitational forces and inertia effects are neglected):

$$\nabla . \boldsymbol{\sigma} = 0. \tag{1}$$

The total stress $\boldsymbol{\sigma}$ in the above equation is related to the effective stress $\boldsymbol{\sigma}'$ and the pore pressure $p_f$ through the Biot's effective stress concept (i.e. $\boldsymbol{\sigma} = \boldsymbol{\sigma}' + \alpha_b p_f \boldsymbol{I}$; $\alpha_b$: Biot coefficient). The changes in the effective stress value $\boldsymbol{\sigma}'$ in both the intact rock and the fracture domain are governed by the selected mechanical constitutive models. In this study, the intact granite was modeled as an isotropic linear elastic material (i.e. Hooke's law defined through two elastic parameters Young's modulus $E$ and Poisson's ratio $\nu$). Additionally, a slip-weakening Mohr–Coulomb plastic model was used to describe the frictional strength, shear-induced dilation and irreversible deformation in the fracture zone. The Mohr–Coulomb yield criterion (onset of plastic shear deformation) is generally defined as follows:

$$\tau = \tan\phi \ \sigma_n' + c \tag{2}$$

where, $\tau$ is the shear stress and $\sigma_n'$ is the effective normal stress on the fracture plane. The parameters $\phi$ and $c$ are the friction angle and the cohesion, respectively. It was assumed that, upon reaching the failure criterion in Eq. (2), the friction angle decreases from its initial static value $\phi_0$ to a residual value $\phi_r$ due to shear sliding. The following exponential function was used to describe the slip-weakening behavior:

$$\phi = \phi_r + (\phi_0 - \phi_r)\exp(-R\ \varepsilon_{ps}) \tag{3}$$

where $\varepsilon_{ps}$ is the plastic shear strain and $R$ is a parameter that controls the rate of friction weakening (Fig. 4(a)). We acknowledge that this method is mesh-dependent, regularization methods could be used to tackle this effect.

Shear failure induced dilation is represented by the dilation angle, $\psi$, which controls the magnitude of the volumetric strain during plastic deformation. The Mohr–Coulomb plastic strain is generally defined as follows:

$$\varepsilon^p = \lambda \ \frac{\partial g}{\partial \sigma} \tag{4}$$

where, $\varepsilon^p$ is the plastic strain, $\lambda$ is the lagrange multiplier and g the plastic flow potential. The plastic flow potential in Mohr–Coulomb is generally defined as:

$$g = \tan\psi \ \sigma_n' + c \tag{5}$$

where, $\tau$ is the shear stress and $\sigma_n'$ is the effective normal stress on the fracture plane. The parameters $\psi$ and c are the dilation angle and the cohesion, respectively. It was assumed that the friction angle is superior to the dilation angle, therefore the flow rule is non-associated.

#### 2.2.2. Hydraulic formulations

The equation for the mass balance of liquids in a porous medium is generally defined as:

$$\left(\frac{\partial \varepsilon_{vol}}{\partial t} + \frac{\partial}{\partial t}\right)(n\ \rho_f) + \nabla \cdot \boldsymbol{q}_f - q^* = 0.0, \tag{6}$$

where $q^*$ is the source term (injection), $n$ the porosity, $\rho_f$ fluid density. The term $\varepsilon_{vol}$ is the volumetric strain, which is a coupling term showing the effect of mechanical deformation on the water pressure. Assuming a constant bulk modulus for water ($K_f = 2.0$ GPa), the following equation was used to describe the changes in water density $\rho_f$ as a function of the pore water pressure $p_f$:

$$\frac{\partial \rho_f}{\partial t} = \frac{\rho_f}{K_f}\frac{\partial p_f}{\partial t} \tag{7}$$

The generalized Darcy's law was used to describe the flow velocity of water $\boldsymbol{q}_f$ (unit: m/s) in Eq. (6) (neglecting gravitational pressure gradient):

$$\boldsymbol{q}_f = -\rho_f \frac{\boldsymbol{k}}{\mu_f} \cdot (\boldsymbol{\nabla} p_f) \tag{8}$$

In the above equation, $p_f$ is the pore pressure (compression positive) and $\mu_f$ is the dynamic viscosity of water. The quantity $\boldsymbol{k}$ is the intrinsic permeability tensor of the medium. In this study, the intact granite was modeled as a low-permeable material with a constant permeability. On the other hand, a permeability function dependent on the hydraulic aperture was taken into account for the fracture zone to replicate the highly non-linear flow rates typically observed during hydro-shearing field experiments (Fig. 4(b)). The cubic-law model developed by Tsang et al. (1981)[22] was used to formulate the permeability of the fracture zone $k_{\text{fracture}}$, assuming a laminar flow within parallel planar fracture surfaces, i.e.

$$k_{\text{fracture}} = \frac{b_h^3}{12} s_f \tag{9}$$

In this equation, $b_h$ is the hydraulic aperture and $s_f$ fracture spacing. The fracture spacing parameter might be useful to estimate the equivalent permeability of a fractured rock medium consisting of a set of persistent fractures with the same spacing and the same apertures.[51] It should be also noted that the substitution of Eq. (9) in Eq. (8) yields directly the volumetric flow rate across the fracture (unit: $m^3/s$). It is well-known that the hydraulic aperture in a fracture may change as a result of mechanical factors such as stress and deformation.[52] Therefore, it was assumed that the hydraulic aperture $b_h$ consists of three parts (as illustrated in Fig. 4(b)), i.e. (1) a constant term $b_{ini}$, (2) a reversible part $b_{el}$ and (3) an irreversible part $b_{shear}$:

$$b_h = b_{ini} + b_{el} + b_{shear} \tag{10}$$

The reversible part of the aperture function was described through the model proposed by Rutqvist et al. (2002).[38,53] According to this model, the reversible hydraulic aperture $b_{el}$ is an exponential function of the effective normal stress $\sigma_n'$ applied to the fracture plane:

$$b_{el} = b_{el}^{max}\exp(\alpha\sigma_n') \tag{11}$$

where, $b_{el}^{max}$, and $\alpha$ are the model parameters, controlling the magnitude and the rate of aperture change as a function of the normal effective

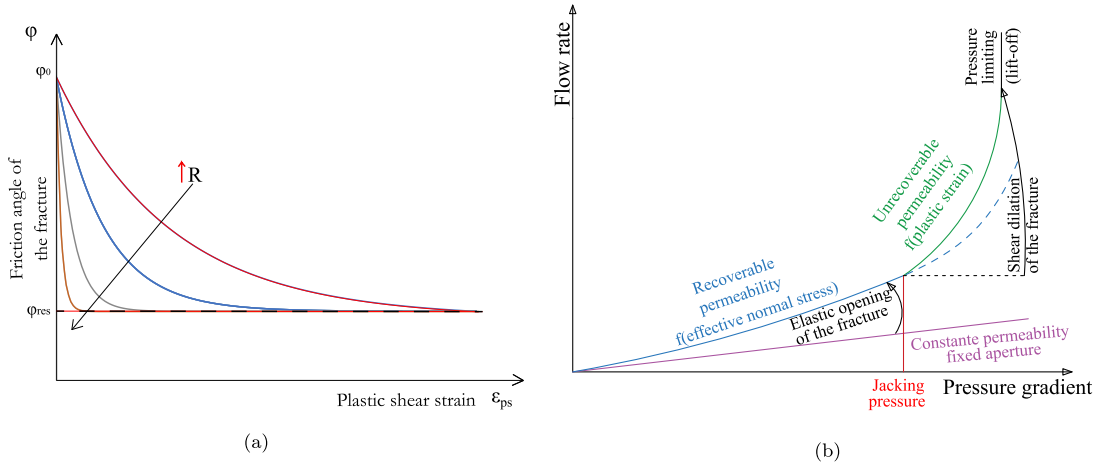


**Fig. 4.** (a) Slip-weakening Mohr–Coulomb model to describe the frictional strength of the fracture zone; (b) Schematic representation of the non-linear flow rate in a fracture as a result of fluid injection, modified after.[50].

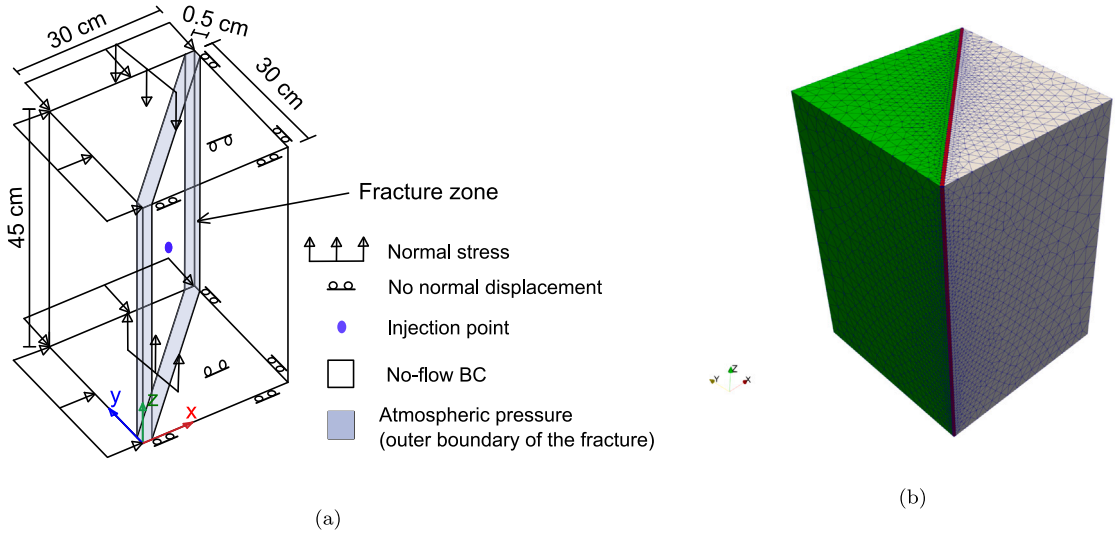


**Fig. 5.** (a) Hydro-mechanical boundary conditions for the numerical modeling of the fluid injection tests; (b) the finite element mesh of the granite block and fracture zone.

stress. The last term in Eq. (10) refers to the changes in hydraulic aperture due to shear slip along the fracture (hydro-shearing). The model proposed by Rinaldi and Rutqvist (2019)[44] was adopted to describe the fracture shear dilation and the resulting changes in hydraulic aperture. Accordingly, the irreversible part of the hydraulic aperture $b_{shear}$ was defined through the equivalent plastic shear strain $\epsilon_{ps}$ and the dilation angle $\psi$:

$$b_{shear} = \max\left(\frac{\epsilon_{ps}\ tan(\psi)}{s_f},\ b_{shear}^{max}\right) \tag{12}$$

The magnitude of equivalent plastic shear strain $\epsilon_{ps}$ depends on the Mohr–Coloumb friction angle defined for the fracture zone, while the irreversible fracture opening is controlled by the dilation angle $\psi$. It should be noted that the irreversible aperture opening $b_{shear}$ was limited to a cut-off parameter $b_{shear}^{max}$. This parameter defines the maximum irreversible opening that can be achieved as a result of shear sliding.

### 2.2.3. 3D FE modeling of the experiments

Fig. 5 presents the geometry of the model and its finite element mesh created in the MOOSE framework. We utilized the Galerkin finite element method employing Lagrange shape functions of first order. For numerical approximation of integrals over the reference element, we employed quadrature techniques, typically utilizing Gaussian Quadrature. Utilizing the MOOSE framework, we have utilized the B-bar approach to mitigate volumetric locking.[54] To address concerns regarding shear locking, we maintained element aspect ratios close to 1 during our investigations. Furthermore, we exercised caution in selecting fracture thickness and final mesh count to prevent the occurrence of very thin elements, which could potentially introduce undesirable numerical artifacts caused by shear-locking.

The fracture zone was modeled using thin 3D continuum elements with an equivalent thickness of 5 mm. We have refined the center of the model at the injection point, specifically focusing on the fracture. At its center, the width of the fracture is represented by 4 elements. Fig. 6 demonstrates the sensitivity of the model to changes in mesh density. As the number of elements increases, particularly in the vicinity of the injection point, the model's accuracy improves. Figs. 6(a) and 6(b) illustrate how the maximum flow rate converges with increasing mesh density and Fig. 6(c) illustrate how the equivalent plastic strain converges with increasing in mesh density. The modeling results remained unchanged as the number of elements exceeded ca. 370000 tetrahedral elements. The final model used for the simulation of the experiments had of ca. 430000 tetrahedral elements and ca. 72000 nodes. With a relatively stable flow rate, dependent on permeability and plastic properties, the model appears appropriately meshed.

Before model calibration, a series of preliminary simulations were carried out to determine a suitable thickness for the fracture zone. Two

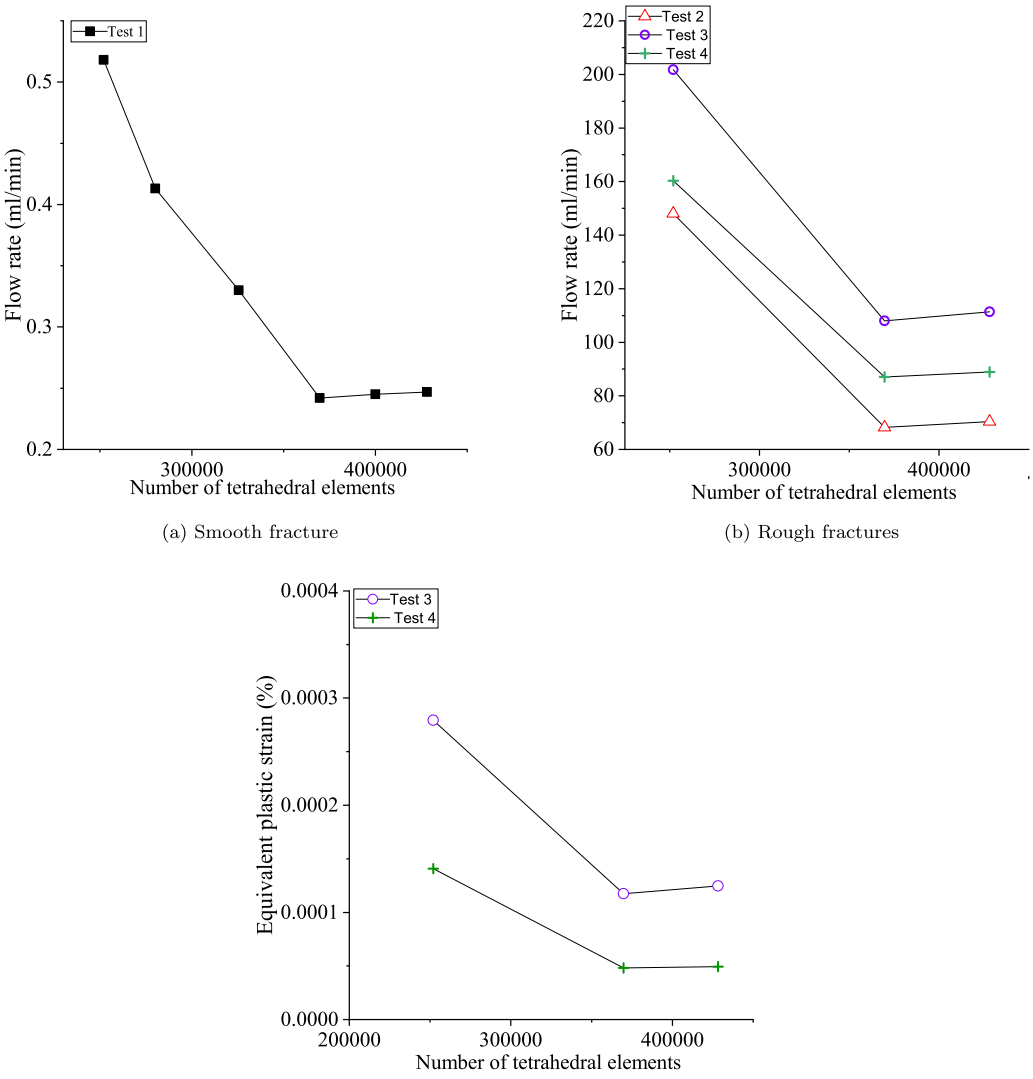


**Fig. 6.** Mesh convergence; (a) Test 1, smooth fracture flow rate; (b) Test 2, 3, 4, rough fracture flow rate; (c) Test 3, 4, rough fracture equivalent plastic strain.

criteria were taken into account to use a reasonable thickness for the fracture zone: (1) ensuring that the fracture zone is not excessively thick to be representative of the problem scale (2) preventing potential numerical problems (e.g., insufficient elements across the thickness, possibly shear-locking due to inappropriate aspect ratio of elemets) associated with an extra thin fracture zone. Moreover, the phenomenon of strain localization results in uneven fluid pressure distributions, significantly influencing the apparent frictional characteristics of the fracture zone and its permeability.[55–58]

The fluid flow was set to zero on the outer boundaries of the granite bulk to define the hydraulic boundary conditions. A constant pressure of 0.1 MPa was applied to the outer boundaries of the fracture zone, considering its connection to the atmosphere. Both the rock and fracture zone were assumed to be fully saturated before and during the experiments. An initial pore pressure of 0.1 MPa was assumed in the entire model. The fracture zone homogenization was idealized as an equivalent porous medium. To compute the equivalent permeability for a single joint, we assumed high porosity, which allows the permeability to be represented as a continuum. This assumption ensures that the equivalent permeability reflects the hydraulic properties of the joint, accounting for the increased flow capacity due to the high porosity. Rutqvist et al. (2020)[59] conducted a comparative study on fracture stimulation techniques, evaluating both continuum and discontinuum methods. Their findings indicate that both approaches adequately reproduce key hydro-mechanical processes within faults. The injection process was modeled as a singular point injection. Fig. 3 also shows the injection pressures applied in the numerical models. The mechanical boundary conditions were defined by constraining one half-block in all directions, while the other half was subjected to constant external loads corresponding to the values implemented in the tests. This approach was used to ensure that the deformations induced within the fracture zone by the injection process (both opening and sliding) remain unaffected by any external mechanical constraints. The goal was to analyze the direct impact of injection, without the interference of additional mechanical influences. The end friction effect resulting from the contrast of elastic properties between steel load plates and the rock samples was not incorporated in the model. The hydro-mechanical properties of intact granite, such as elastic parameters, porosity, and permeability, were primarily derived from previous studies on comparable rocks (e.g.[60,61], Table 1). The model parameters associated with the fracture zone, including both the slip-weakening Mohr–Coulomb model and the aperture-dependent permeability function, were determined through back-calculation by calibrating the model against the conducted laboratory experiments (Tables 1 and 2).

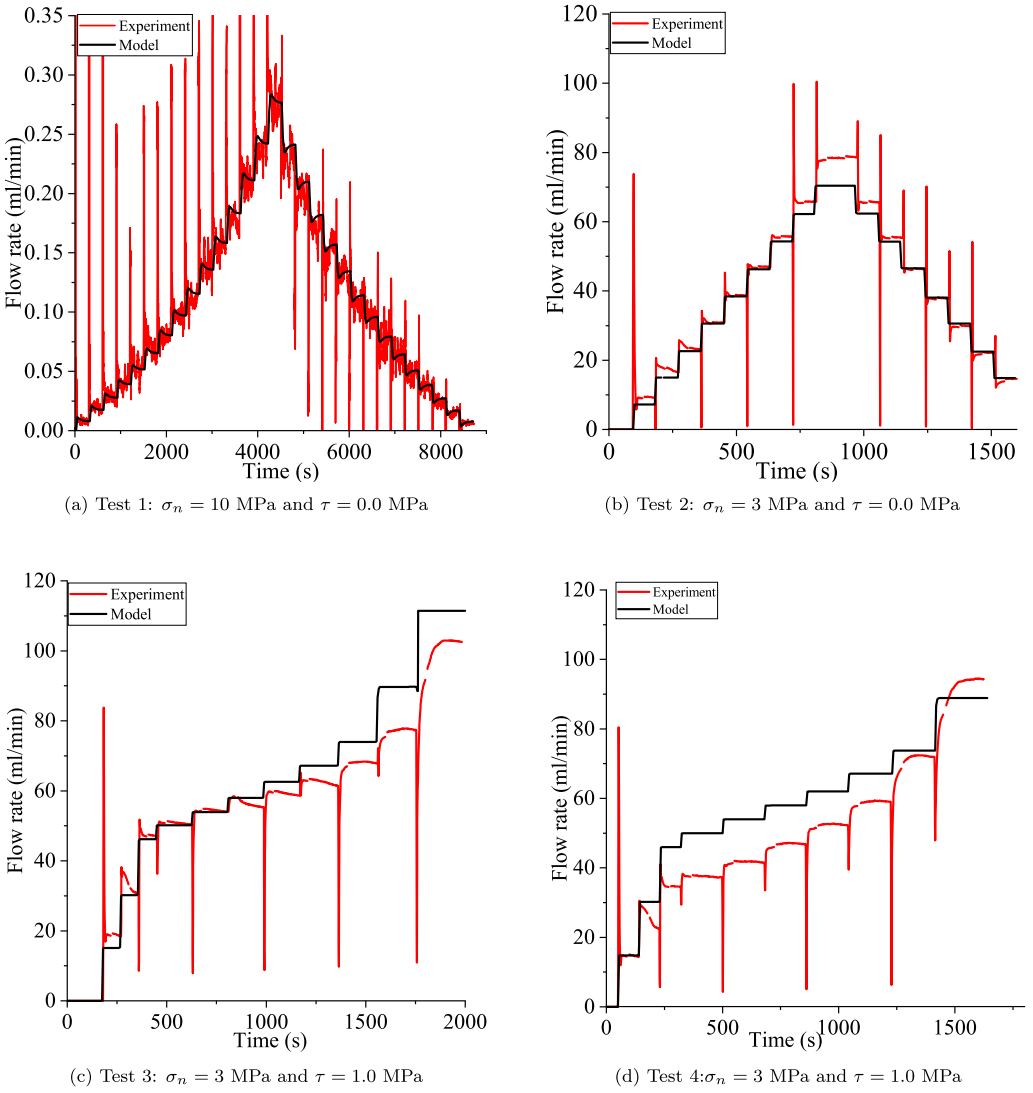


(a) Test 1: $\sigma_n = 10$ MPa and $\tau = 0.0$ MPa

(b) Test 2: $\sigma_n = 3$ MPa and $\tau = 0.0$ MPa

(c) Test 3: $\sigma_n = 3$ MPa and $\tau = 1.0$ MPa

(d) Test 4:$\sigma_n = 3$ MPa and $\tau = 1.0$ MPa

**Fig. 7.** Flow rate evolution obtained during hydraulic stimulation tests along with the numerical modeling results; (a) Test 1, isotropic loading/smooth fracture; (b) Test 2, isotropic loading/rough fracture; (c) Test 3, shear loading/rough fracture; (d) Test 4, shear loading/rough fracture.

**Table 1**
Hydro-mechanical parameters used in the numerical models.

| Parameters | Unit | Granite | Fracture zone |
|---|---|---|---|
| **Mechanical model** | | | |
| Young modulus (E) | GPa | 37 | 37 |
| Poisson's ratio ($\nu$) | – | 0.3 | 0.3 |
| Cohesion ($c$) | MPa | – | 0.0 |
| Static friction angle ($\phi_0$) | ° | – | 37 |
| Residual friction angle ($\phi_r$) | ° | – | 20 |
| Dilation angle ($\psi$) | ° | – | 15 |
| Softening rate (R) | – | – | 3000 |
| **Hydraulic model** | | | |
| Biot coefficient ($\alpha_b$) | – | 1 | 1 |
| Fluid density ($\rho_f$) | kg/m$^3$ | 1000 | 1000 |
| Fluid viscosity ($\mu_f$) | MPa*s | $10^{-9}$ | $10^{-9}$ |
| Fluid bulk modulus ($K_f$) | GPa | 2 | 2 |
| Rock density ($\rho_r$) | kg/m$^3$ | 2640 | 2640 |
| Porosity ($n$) | % | 1.5 | 95 |
| Permeability tensor ($k$) | m$^2$ | $10^{-22}$ | Table 2 |

**Table 2**
Input model parameters for the fracture permeability function.

| Parameters | Unit | Test 1 (smooth) | Test 2 (rough) | Test 3 (rough) | Test 4 (rough) |
|---|---|---|---|---|---|
| $b_{el}^{max}$ | μm | 16.5 | 115 | 115 | 115 |
| $b_{ini}$ | μm | 0.85 | 10 | 10 | 10 |
| $\alpha$ | MPa$^{-1}$ | 0.06 | 0.005 | 0.005 | 0.005 |
| $b_{shear}^{max}$ | μm | – | – | 28 | 28 |
| $s_f$ | m$^{-1}$ | 1 | 1 | 1 | 1 |

## 3. Results and discussion

### 3.1. Injection flow rate versus time

Fig. 7 shows the injection flow rate (unit: mL/min) obtained within the experiments. In the first test, isotropic loading/smooth fracture, the injected flow rate gradually increased to approximately 0.27 mL/min as the injection pressure reached step-wise to a maximum of 15 MPa (Fig. 7(a)). The monitored flow rate showed a sudden increase at the beginning of each pressure interval followed by a rapid decrease to a steady-state value. The large fluctuations observed in the flow rate were probably due to low injectivity which made the pump regulation

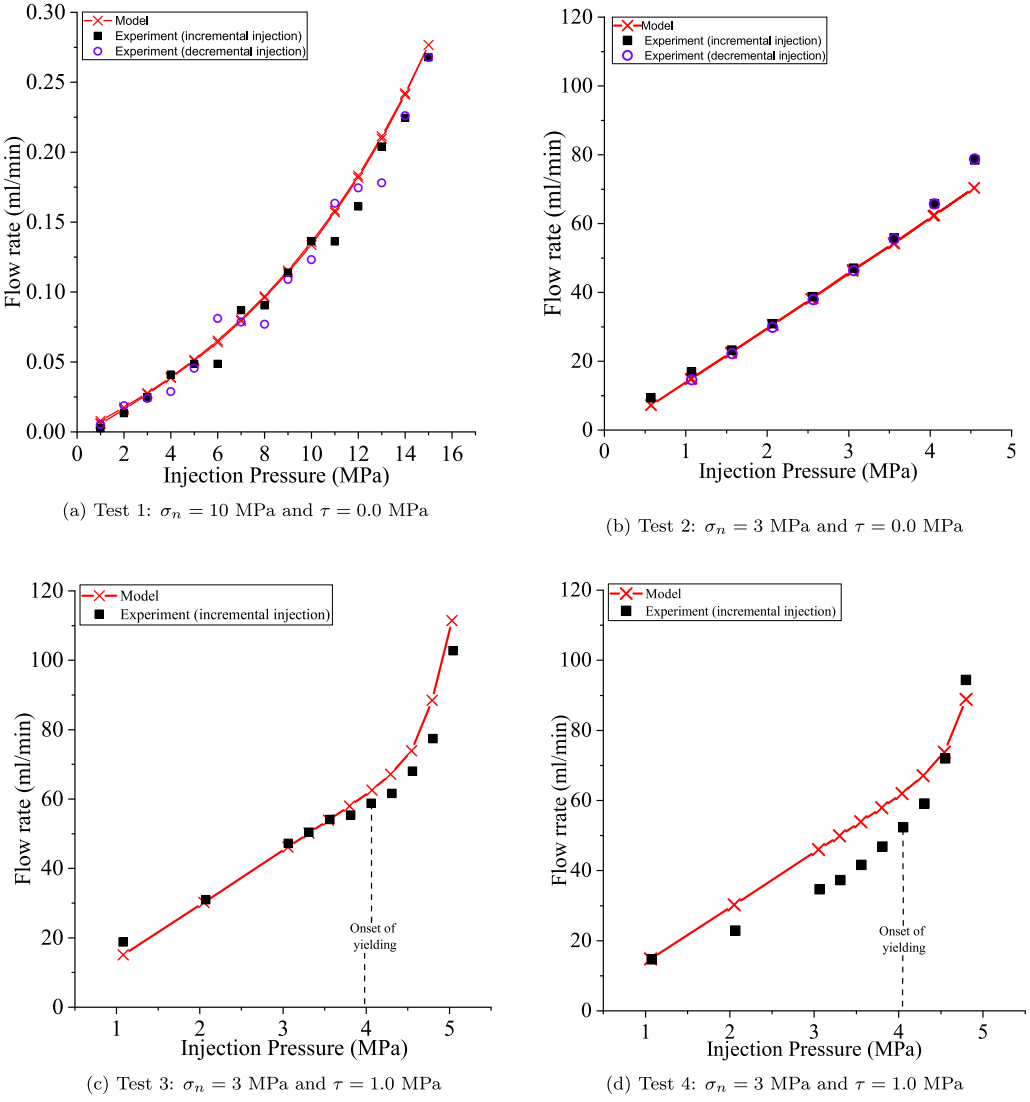


(a) Test 1: $\sigma_n = 10$ MPa and $\tau = 0.0$ MPa

(b) Test 2: $\sigma_n = 3$ MPa and $\tau = 0.0$ MPa

(c) Test 3: $\sigma_n = 3$ MPa and $\tau = 1.0$ MPa

(d) Test 4: $\sigma_n = 3$ MPa and $\tau = 1.0$ MPa

**Fig. 8.** Flow rate versus injection pressure along with the numerical modeling results; (a) Test 1, isotropic loading/smooth fracture; (b) Test 2, isotropic loading/rough fracture; (c) Test 3, shear loading/rough fracture; (d) Test 4, shear loading/rough fracture.

difficult. During the pressure recovery stage, as the pressure reduced to zero, the obtained flow rates were nearly identical to those observed during the injection stage for the same injection pressure. This observation indicates a reversible opening/closure mechanism in the fracture. The maximum flow rate achieved at the injection pressure of 15 MPa was very small (about 0.27 mL/min), indicating a minimal hydraulic aperture of the fracture due to the small asperities at the fracture plane and the high isotropic confining stress applied to the sample. The impact of these two factors, i.e. applied confining stress and fracture roughness, on the hydraulic flow paths was highlighted in the results of the second test (Fig. 7(b)). In this test, the larger asperities on the rough fracture plane created a more substantial flow path along the fracture. The injection flow rate monitored during the test reached 80 mL/min when the injection pressure was almost 4.5 MPa (i.e., almost 2 orders of magnitude larger than in the first test). The flow rate values in their steady-state condition exhibited a consistent increase of around 8 mL/min per constant pressure increment of 0.5 MPa. This observation suggests that while there may not have been a significant absolute aperture change compared to Test 1, while there may not have been a significant absolute aperture change compared to Test 1, the relative permeability gain was not substantial due to the already high initial permeability. In the last two tests, the impact of injection-induced shear slip on the flow rate evolution was investigated, where the fracture was subjected to a pre-defined shear stress of $\tau$=1 MPa (Figs. 7(c) and 7(c)). Although the normal stresses applied to the fracture surface in the last two tests were similar to that of Test 2, the flow rate experienced a significant increase during the final pressure increment, rising from around 80 mL/min to a value surpassing 100 mL/min. This rapid increase in the injection flow rate was probably associated with the development of larger flow paths resulting from shear slip and dilation.

The results of the numerical models are also depicted in Fig. 7. In the absence of shear loading, the hydraulic aperture function in Eq. (10) includes only the initial and reversible terms ($b_{ini}$, $b_{el}$). The testing results of isotropically loaded samples (tests 1 and 2) were utilized to back-calculate the parameters required for the initial and reversible hydraulic aperture model for both smooth and rough surfaces. On the other hand, the flow rate evolution in Tests 3 and 4 were adopted to estimate the irreversible term of hydraulic aperture function $b_{shear}$ as well as the frictional properties of the fracture zone. The model calibration resulted in two different sets of parameters for the smooth and rough fracture surfaces (Tables 1 and 2). The aperture is an equivalent effective aperture computed alongside the equivalent permeabilities using the cubic law.

In Test 1, the numerical maximum flow rate is 3.6% lower than the experimental value. However, overall, the experiment and test

exhibited a similar trend. For Test 2, the numerical maximum flow rate is 11.8% lower than the experimental one. Despite this, the experiment and test generally followed a close trend, with some discrepancies noted particularly at an injection pressure of 4 MPa. Test 3 showed a numerical maximum flow rate 8.4% higher than the experimental value. Although the experiment and test generally followed a similar trend, there were some deviations, especially noticeable at an injection pressure of 3.8 MPa. This discrepancy tended to increase with higher injection pressures. In Test 4, the numerical maximum flow rate is 5.8% lower than the experimental one. Overall, the experiment and test exhibited some deviation, especially notable at an injection pressure of 3 MPa. However, as shearing commenced, the model and experiment became more aligned. The model's testing is confined to a specific range of stresses and fluxes. The maximum injection pressure reaches 15 MPa for a smooth fracture and 4.5 MPa for a rough fracture. The stress range varies from 10 MPa for a smooth fracture to 3 MPa for a rough fracture. These values represent a subset of realistic hydraulic, tectonic and gravitational stress ranges that could occur in certain reservoirs.

### 3.2. Flow rate versus injection pressure

The relationship between injection pressure and the resulting flow rate is depicted in Fig. 8. In the first test, the flow rate showed a linear increase up to an injection pressure of nearly 4 MPa, indicating a constant hydraulic aperture within this pressure range. However, beyond 4 MPa, the flow rate curve deviated from linearity and gradually increased as the injection pressure elevated to 15 MPa (Fig. 8(a)). Since no shear stress was applied in this test, the deviation from linearity is likely a result of the normal opening and closure of the fracture induced by the high injection pressure. During the pressure recovery phase, the flow rate values followed the same nonlinear curve, indicating the reversibility of the process. The model incorporated the aperture function $b_{el}$ in Eq. (11) to describe the reversible nonlinear evolution of flow rate as a result of changes in the effective normal stress on the fracture plane. However, this non-linear evolution of flow rate was not observed in the second test. The results exhibited an almost perfectly linear increase in flow rate up to an injection pressure of 4.5 MPa (Fig. 8(b)). This observation suggests that mechanical deformations in the fracture, such as opening and closure, had a negligible impact on hydraulic behavior. Two key factors support this observation: (1) the injection pressure was not sufficiently high to substantially open the fracture, and (2) the shear stress on the fracture plane was zero in this test (no sliding). Figs. 8(c) and 8(d) depict the flow rate-pressure curves for the injection tests on rough fractures subjected to a predefined shear stress. In both experiments, the flow rate exhibited an almost linear increase with the rising injection pressure, up to a pressure of almost 4.5 MPa (similar to test3). Subsequently, a pronounced and rapid increase in flow rate occurred as the pressure approached 5 MPa. The rate of change in flow curve was notably higher than that observed in the first test. Hence, this abrupt rise in flow is thought to be due to shear slip, inducing self-propping on asperities (dilation) and consequently leading to an irreversible increase in flow rate.

### 3.3. Injection-induced permeability change

During the experiments, the hydraulic parameters such as hydraulic aperture and fracture permeability were not directly measured. Instead, these parameters were inferred from numerical modeling results, calibrated using other measurable quantities including flow rate and pressure. Figs. 9 and 11 illustrate changes in hydraulic aperture values and resulting permeabilities around the injection point derived from the numerical modeling results. The quantity $b_{\text{normal}}$ in these figures represents the summation of the initial and reversible terms of the aperture function, i.e., $b_{\text{normal}} = b_{\text{ini}} + b_{\text{el}}$. Figs. 9(a) and 9(b) depict changes in $b_{\text{normal}}$ in tests 1 and 2, respectively ($b_{\text{shear}}$ was zero in the absence of shearing). In the first test, the hydraulic aperture $b_{\text{normal}}$ increased from the initial value of 10 μm to 14 μm as the injection pressure reached 15 MPa. A similar increase in hydraulic aperture $b_{\text{normal}}$ was obtained by the model for the second test, i.e., from the initial value of 120 μm to 123 μm for a pressure increase of 4.5 MPa. The back-calculated hydraulic aperture for the rough fracture surface was nearly one order of magnitude larger than that of the smooth fracture, explaining the possible reason for the substantially different flow rates observed in Tests 1 and 2. In addition, the relative change in hydraulic aperture for the rough fracture, i.e., the ratio between the aperture opening and the initial hydraulic aperture, was much smaller than that of the smooth fracture. Consequently, the induced changes in aperture were expected to have a minor influence on permeability in Test 2. The permeability evolution in tests 1 and 2 around the injection point are depicted in Figs. 9(c) and 9(d), respectively. The back-calculated permeability of the rough fracture was almost 3 orders of magnitude larger than the permeability of smooth fracture. For the smooth fracture, the fracture permeability increased from 9.0e−17$m^2$ to 2.1e−16 $m^2$ (almost double), while for the rough fracture, permeability remained almost constant at approximately 1.5e−13 $m^2$. The changes in effective normal stress at the injection point on the fracture plane have been also shown in Figs. 9(c) and 9(d). In both cases, the effective normal stress decreased during the fluid injection phase, followed by a reversible increase during the pressure recovery phase. Figs. 10(a) and 10(b) illustrate how the aperture changes around the injection point based on the effective normal stress for both smooth and rough fractures. In a smoother fracture, the asperities (roughness) are smaller, resulting in a smaller aperture when two blocks come into contact, as compared to a rough fracture with larger asperities. Additionally, due to the higher initial stress and smoother fracture walls, the initial aperture is lower in smooth fractures, and the relative change in aperture with stress variation is more pronounced compared to rough fractures. For instance, when the effective normal stress drops by approximately 185%, the aperture of a smooth fracture increases by about 40%, whereas for a rough fracture, a drop of about 114% in effective normal stress leads to only a 2.25% increase in aperture. Consequently, the opening and closing behavior of a rough fracture is significantly less than that of a smooth fracture due to differences in their stiffness.

In Tests 3 and 4, the total hydraulic aperture includes both $b_{\text{normal}}$ and $b_{shear}$ terms. The evolution of these terms are shown in Figs. 11(a) and 11(b). The magnitude of changes in $b_{\text{normal}}$ obtained for tests 3 and 4 was similar to that of Test 2, given the nearly identical surface roughness and injection protocols in these tests. However, a rapid increase in the irreversible part of hydraulic aperture, $b_{\text{shear}}$, was obtained when the injection pressure exceeded almost 4 MPa. This abrupt increase in $b_{\text{shear}}$ resulted from plastic shear strain around the injection point, leading to dilation and subsequently irreversible shear-induced opening. In Test 3, an increase of almost 27 μm was obtained for the irreversible hydraulic aperture $b_{\text{shear}}$ when the injection pressure reached 5 MPa (Fig. 11(a)). The calculated $b_{\text{shear}}$ value at the peak pressure in Test 4 was lower than in Test 3, but the rapid increase was still remarkable (Fig. 11(b)). Figs. 11(c) and 11(d) show the changes in effective normal stress at the injection point and resulting permeability for Tests 3 and 4, respectively. The permeability increase in Test 3 was more pronounced, likely due to the lower normal stress reached and higher plastic strain.

The permeability value increased by almost twofold in this experiment. Fig. 12(a) depicts the contour plot of effective normal stress $\sigma_n'$ on the fracture plane for Test 3, obtained from the numerical modeling. As illustrated, there is a high gradient in the normal stress distribution around the injection point. Fig. 12(b) displays the distribution of effective normal stress value along a horizontal line along the fracture. The remarkable normal stress gradient results from the fracture's connection to the atmosphere, leading to a substantial fluid pressure gradient from the injection point towards the fracture boundaries. The lowest value of effective normal stress is obtained around the injection point, where the fluid pressure is highest. As

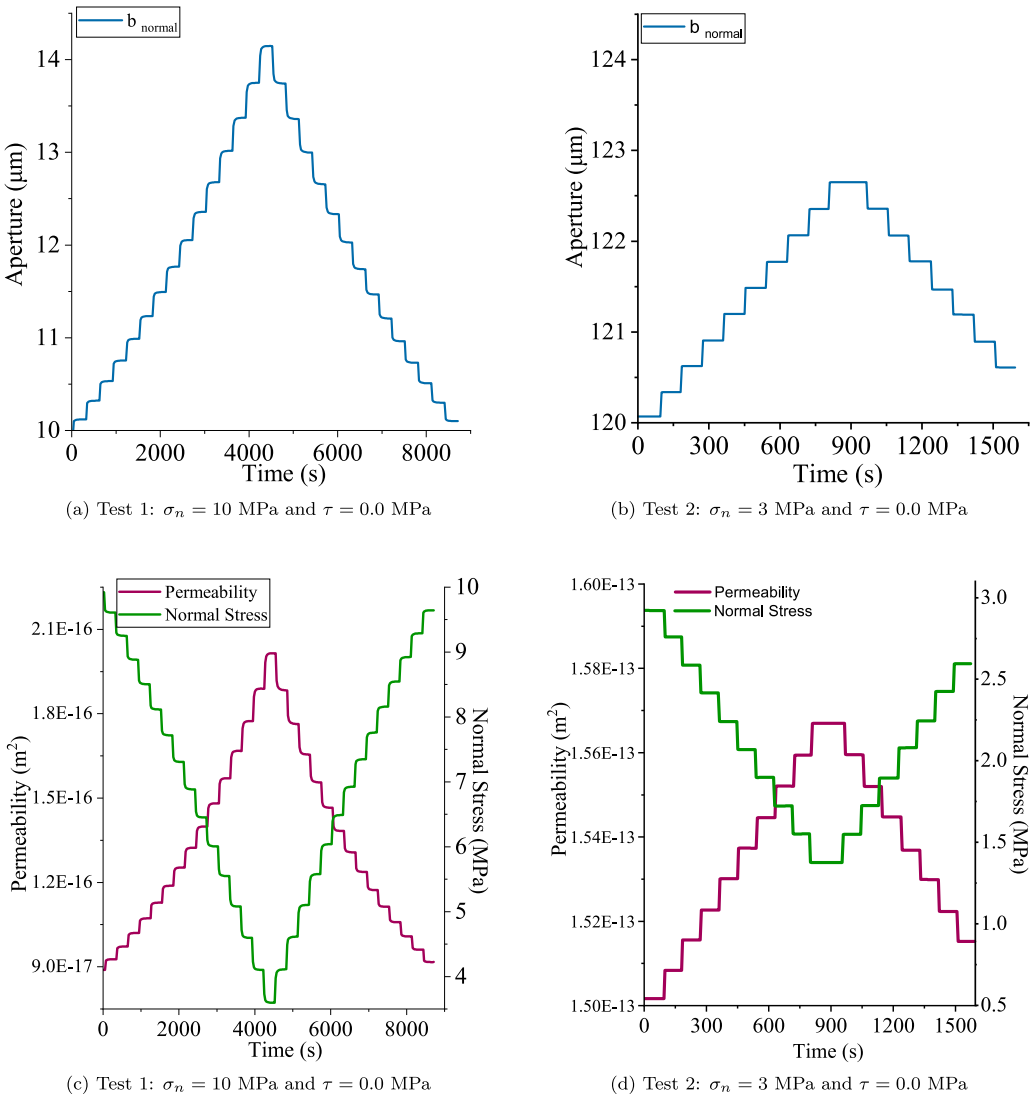


(a) Test 1: $\sigma_n = 10$ MPa and $\tau = 0.0$ MPa

(b) Test 2: $\sigma_n = 3$ MPa and $\tau = 0.0$ MPa

(c) Test 1: $\sigma_n = 10$ MPa and $\tau = 0.0$ MPa

(d) Test 2: $\sigma_n = 3$ MPa and $\tau = 0.0$ MPa

**Fig. 9.** Changes in hydraulic aperture and permeability of fracture obtained from numerical modeling; (a) hydraulic aperture in Test 1, isotropic loading/smooth fracture; (b) hydraulic aperture in Test 2, isotropic loading/rough fracture; (c) permeability in Test 1, isotropic loading/smooth fracture; (d) permeability in Test 2, isotropic loading/rough fracture.

shown in Fig. 12(c), theoretically, the onset of plastic dilation occurs when the effective normal stress on the fracture plane reduces to a value of 1.4 MPa (assuming a friction angle of 37°, Table 1). Under this stress condition, the Mohr–Coulomb plastic yield criteria were satisfied, leading to the initiation of shear-induced dilation. The contour plot of $b_{\text{shear}}$ parameter on the fracture plane is shown in Fig. 12(d) (for Test 3). The distribution of this parameter is directly correlated with the plastic strain developed along the fracture plane. Modeling results indicate that shear-induced dilation and irreversible aperture increase are localized within a small zone, with a diameter of 8.4 mm, around the injection point. The size and distribution of the plastic dilation zone depend on the effective stress distribution on the fracture plane. As indicated in Fig. 12(b), only a small zone, approximately 8.4 mm in diameter, experiences an effective normal stress less than 1.4 MPa.

## 4. Summary and conclusion

Understanding the evolution of fracture permeability is crucial for characterizing fluid transport in fractured rocks and developing strategies to enhance the productivity during hydraulic stimulation of geothermal reservoirs. An important factor in this context is how fluid pressure affects permeability. In this study, we conducted a series of laboratory experiments with pressure-controlled injection into smooth and rough fractures in granite under pre-stressed conditions. A coupled hydro-mechanical modeling framework was employed to describe the permeability of fracture taking into account the changes in hydraulic aperture as a function of effective normal stress and plastic shear-induced dilation. Moreover, a slip-weakening Mohr–Coulomb model was used to describe the progressive shear slide under compression and the post-failure behavior of pre-existing fractures.

The study involved deriving hydraulic parameters, such as hydraulic aperture and fracture permeability, from numerical modeling results calibrated with measurable quantities like flow rate and pressure. The experiments showed substantial differences in flow rate evolution between smooth and rough fractures, highlighting the important role of fracture asperities on the permeability. Additionally, the tests with predefined shear stress on the fracture plane exhibited notable increases in irreversible permeability due to plastic shear strain, leading to significant slide-induced dilation, showing a nearly twofold increase in permeability. The roughness of a fracture influences the changes in

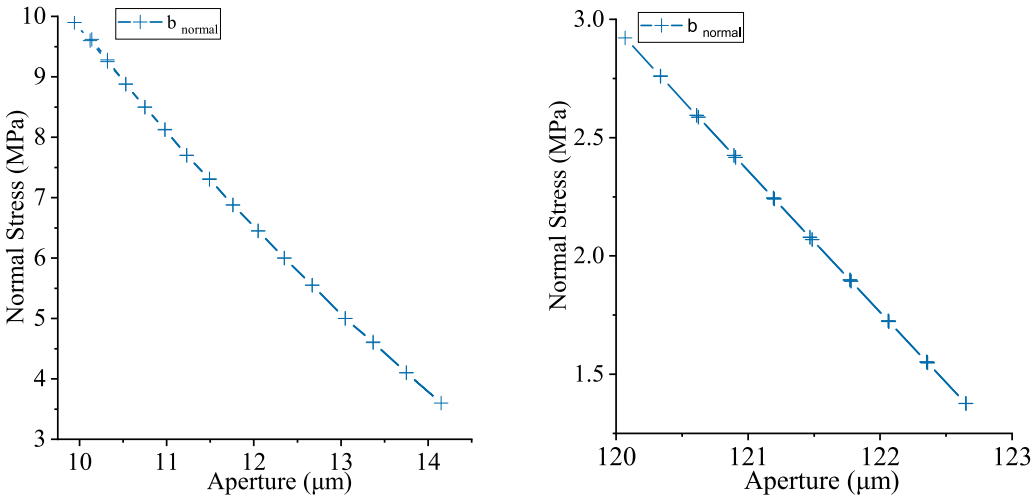


(a) Test 1: $\sigma_n = 10$ MPa and $\tau = 0.0$ MPa (b) Test 2: $\sigma_n = 3$ MPa and $\tau = 0.0$ MPa

**Fig. 10.** Changes in hydraulic aperture and effective normal stress obtained from numerical modeling; (a) hydraulic aperture in Test 1, isotropic loading/smooth fracture; (b) hydraulic aperture in Test 2.

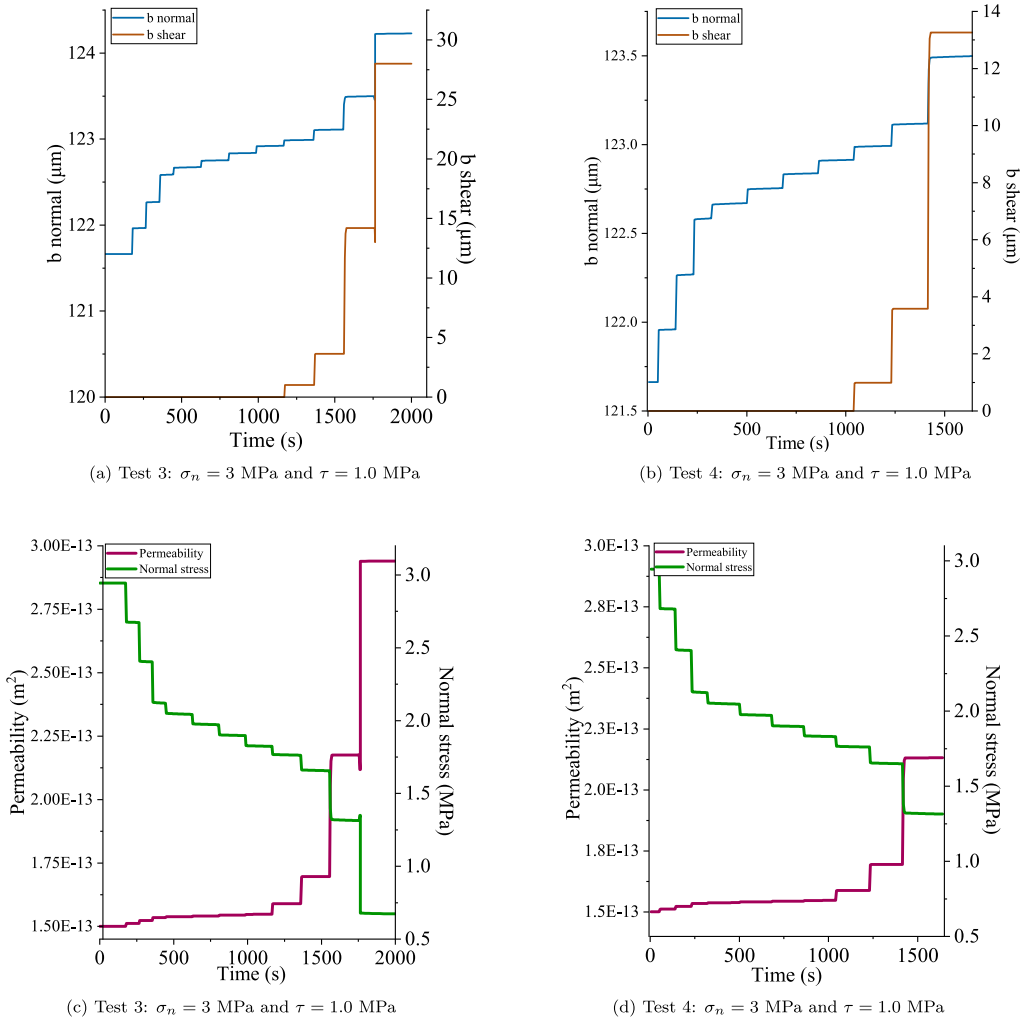


(a) Test 3: $\sigma_n = 3$ MPa and $\tau = 1.0$ MPa (b) Test 4: $\sigma_n = 3$ MPa and $\tau = 1.0$ MPa

(c) Test 3: $\sigma_n = 3$ MPa and $\tau = 1.0$ MPa (d) Test 4: $\sigma_n = 3$ MPa and $\tau = 1.0$ MPa

**Fig. 11.** Changes in hydraulic aperture and permeability of rough fracture obtained from numerical modeling; (a) hydraulic aperture in Test 3; (b) hydraulic aperture in Test 4; (c) permeability change in Test 3; (d) permeability change in Test 4.

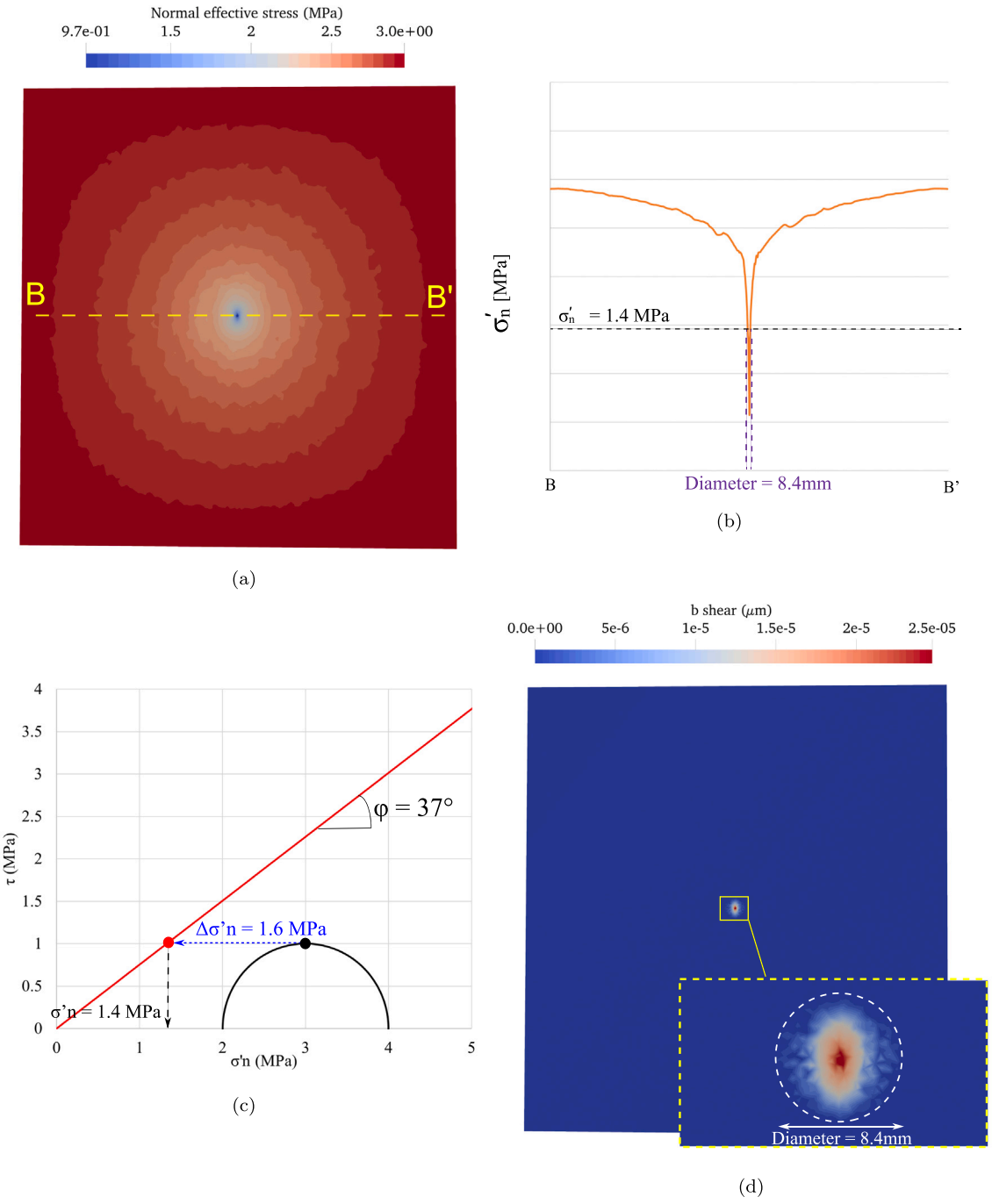


**Fig. 12.** (a) The contour plot of normal effective stress on the fracture plane for Test 3; (b) the distribution of normal effective stress along a horizontal line passing through; (c) the initial effective stress state in Test 3 and the required condition to satisfy the Mohr–Coulomb failure condition; (d) the fracture A vertical cut though the fracture showing contour plot $b_{shear}$ value in Test 3.

permeability induced by fluid injection. Rough fractures exhibit fewer changes during stimulation compared to smooth fractures. However, initiating shear sliding in smooth fractures is more complex. Additional sources of complexity include thermo-hydro-chemo-mechanical effects, creep, and heterogeneities can alter the fracture behavior. To tackle these challenges, an extension of the experimental setup and numerical framework is necessary. For example, a more detailed analysis of the fracture surface topography before and after a test could help to assess stress heterogeneity and validate the permanent aperture changes. Further research in this direction is imperative to explore various scenarios and derive useful, quantitative conclusions applicable to real-world reservoir.

## CRediT authorship contribution statement

**Josselin Ouf:** Writing – review & editing, Writing – original draft, Visualization, Methodology, Investigation, Formal analysis, Data curation, Conceptualization. **Julian Osten:** Writing – review & editing, Visualization, Resources, Methodology, Investigation, Data curation. **Wen Luo:** Writing – review & editing, Methodology, Investigation. **Kavan Khaledi:** Writing – original draft, Visualization, Supervision, Methodology, Investigation, Formal analysis, Data curation, Conceptualization. **Mohammadreza Jalali:** Writing – review & editing, Supervision, Methodology, Investigation. **Philip J. Vardon:** Writing – review

& editing, Methodology, Funding acquisition, Formal analysis, Conceptualization. **Florian Amann:** Writing – review & editing, Methodology, Investigation, Funding acquisition, Formal analysis, Conceptualization.

## Declaration of competing interest

The authors declare that they have no known competing financial interests or personal relationships that could have appeared to influence the work reported in this paper.

## Data availability

No data was used for the research described in the article.

## Acknowledgments

This work was performed in the framework of the EAGYGO-ITN project. The authors are thankful for the financial support received from the European Union's Horizon 2020 research and innovation program under the Marie-Curie grant agreement No 956965. The authors thank Dr. Max Kewel and the laboratory staff at the Chair of Geotechnical Engineering and Institute of Geomechanics and Underground Technology (GuT), RWTH Aachen University for their contribution to the experimental works. We also thanks two anonymous reviewer for their helpful reviews.

## References

1. Saar OM. *Novel Geothermal Technologies, in: Potentials, Costs and Environmental Assessment of Electricity Generation Technologies*. Tech. Rep. Swiss Federal Office of Energy, Swiss Competences Center for Energy Research "Supply of Electricity" and "Biomass for Swiss Energy Future", Bern, Switzerland; 2017.
2. Lu S-M. A global review of enhanced geothermal system (EGS). *Renew Sustain Energy Rev*. 2018;81:2902–2921.
3. Saar MO, Manga M. Depth dependence of permeability in the oregon cascades inferred from hydrogeologic, thermal, seismic, and magmatic modeling constraints. *J Geophys Res Solid Earth*. 2004;109(B4).
4. Achtziger-Zupančič P, Loew S, Mariethoz G. A new global database to improve predictions of permeability distribution in crystalline rocks at site scale. *J Geophys Res Solid Earth*. 2017;122(5):3513–3539.
5. Gischig VS, Giardini D, Amann F, et al Hydraulic stimulation and fluid circulation experiments in underground laboratories: Stepping up the scale towards engineered geothermal systems. *Geomech Energy Environ*. 2020;24:100175.
6. Amann F, Gischig V, Evans K, et al The seismo-hydromechanical behavior during deep geothermal reservoir stimulations: open questions tackled in a decameter-scale in situ stimulation experiment. *Solid Earth*. 2018;9(1):115–137.
7. Evans KF, Moriya H, Niitsuma H, et al Microseismicity and permeability enhancement of hydrogeologic structures during massive fluid injections into granite at 3 km depth at the soultz HDR site. *Geophys J Int*. 2005;160(1):388–412.
8. Gérard A, Genter A, Kohl T, Lutz P, Rose P, Rummel F. The deep EGS (enhanced geothermal system) project at Soultz-sous-Forêts (Alsace, France). *Geothermics*. 2006;35(5):473–483.
9. Bendall B, Hogarth R, Holl H, McMahon A, Larking A, Reid P. Australian experiences in EGS permeability enhancement–a review of 3 case studies. In: *Thirty-Ninth Workshop on Geothermal Reservoir Engineering, Stanford University*. 2014.
10. Kelkar S, WoldeGabriel G, Rehfeldt K. Lessons learned from the pioneering hot dry rock project at Fenton Hill, USA. *Geothermics*. 2016;63:5–14.
11. Brown D. The US hot dry rock program-20 years of experience in reservoir testing. In: *Proceedings of the World Geothermal Congress, Vol. 4*. 1995:2607–2611.
12. Kim K-H, Ree J-H, Kim Y, Kim S, Kang SY, Seo W. Assessing whether the 2017 M w 5.4 pohang earthquake in South Korea was an induced event. *Science*. 2018;360(6392):1007–1009.
13. Häring MO, Schanz U, Ladner F, Dyer BC. Characterisation of the basel 1 enhanced geothermal system. *Geothermics*. 2008;37(5):469–495.
14. Schmittbuhl J, Lambotte S, Lengliné O, et al Induced and triggered seismicity below the city of Strasbourg, France from November 2019 to January 2021. *C R Géosci*. 2021;353(S1):561–584.
15. Kukkonen IT, Heikkinen PJ, Malin PE, et al Hydraulic conductivity of the crystalline crust: Insights from hydraulic stimulation and induced seismicity of an enhanced geothermal system pilot reservoir at 6 km depth, Espoo, southern Finland. *Geothermics*. 2023;112:102743.
16. Kivi IR, Boyet A, Wu H, et al Global physics-based database of injection-induced seismicity. *Earth Syst Sci Data Discuss*. 2023;2023:1–33.
17. McClure MW, Horne RN. An investigation of stimulation mechanisms in enhanced geothermal systems. *Int J Rock Mech Min Sci*. 2014;72:242–260.
18. Guglielmi Y, Birkholzer J, Rutqvist J, Jeanne P, Nussbaum C. Can fault leakage occur before or without reactivation? Results from an in situ fault reactivation experiment at Mont Terri. *Energy Procedia*. 2017;114:3167–3174.
19. Guglielmi Y, Nussbaum C, Cappa F, De Barros L, Rutqvist J, Birkholzer J. Field-scale fault reactivation experiments by fluid injection highlight aseismic leakage in caprock analogs: Implications for CO2 sequestration. *Int J Greenh Gas Control*. 2021;111:103471.
20. Jeanne P, Guglielmi Y, Rutqvist J, Nussbaum C, Birkholzer J. Permeability variations associated with fault reactivation in a claystone formation investigated by field experiments and numerical simulations. *J Geophys Res Solid Earth*. 2018;123(2):1694–1710.
21. Barton N. Review of a new shear-strength criterion for rock joints. *Eng Geol*. 1973;7(4):287–332.
22. Tsang YW, Witherspoon P. Hydromechanical behavior of a deformable rock fracture subject to normal stress. *J Geophys Res Solid Earth*. 1981;86(B10):9287–9298.
23. Gentier S, Riss J, Archambault G, Flamand R, Hopkins D. Influence of fracture geometry on shear behavior. *Int J Rock Mech Min Sci*. 2000;37(1–2):161–174.
24. Sausse J. Hydromechanical properties and alteration of natural fracture surfaces in the Soultz granite (Bas-Rhin, France). *Tectonophysics*. 2002;348(1–3):169–185.
25. Zoback M, Rummel F, Jung R, Raleigh C. Laboratory hydraulic fracturing experiments in intact and pre-fractured rock. (no. 2):Elsevier; 1977:49–58. In: International Journal of Rock Mechanics and Mining Sciences & Geomechanics Abstracts; vol. 14.
26. Deb P, Düber S, Guarnieri Calo'Carducci C, Clauser C. Laboratory-scale hydraulic fracturing dataset for benchmarking of enhanced geothermal system simulation tools. *Sci Data*. 2020;7(1):220.
27. Zhang F, An M, Zhang L, Fang Y, Elsworth D. Effect of mineralogy on friction-dilation relationships for simulated faults: Implications for permeability evolution in caprock faults. *Geosci Front*. 2020;11(2):439–450.
28. Wang L, Kwiatek G, Bohnhoff M, Rybacki E, Dresen G. Injection-induced fault slip and associated seismicity in the lab: Insights from source mechanisms, local stress states and fault geometry. *Earth Planet Sci Lett*. 2024;626:118515.
29. Ye Z, Ghassemi A. Injection-induced shear slip and permeability enhancement in granite fractures. *J Geophys Res Solid Earth*. 2018;123(10):9009–9032.
30. Ishibashi T, Elsworth D, Fang Y, et al Friction-stability-permeability evolution of a fracture in granite. *Water Resour Res*. 2018;54(12):9901–9918.
31. Li Z, Ma X, Kong X-Z, Saar MO, Vogler D. Permeability evolution during pressure-controlled shear slip in saw-cut and natural granite fractures. *Rock Mech Bull*. 2023;2(2):100027.
32. Almakari M, Chauris H, Passelègue F, Dublanchet P, Gesret A. Fault's hydraulic diffusivity enhancement during injection induced fault reactivation: application of pore pressure diffusion inversions to laboratory injection experiments. *Geophys J Int*. 2020;223(3):2117–2132.
33. Pandey S, Vishal V, Chaudhuri A. Geothermal reservoir modeling in a coupled thermo-hydro-mechanical-chemical approach: A review. *Earth-Sci Rev*. 2018;185:1157–1169.
34. Park J-W, Guglielmi Y, Graupner B, et al Modeling of fluid injection-induced fault reactivation using coupled fluid flow and mechanical interface model. *Int J Rock Mech Min Sci*. 2020;132:104373.
35. Cappa F, Guglielmi Y, Nussbaum C, De Barros L, Birkholzer J. Fluid migration in low-permeability faults driven by decoupling of fault slip and opening. *Nat Geosci*. 2022;15(9):747–751.
36. Rutqvist J, Rinaldi AP, Cappa F, Moridis GJ. Modeling of fault reactivation and induced seismicity during hydraulic fracturing of shale-gas reservoirs. *J Pet Sci Eng*. 2013;107:31–44.
37. Rutqvist J, Rinaldi AP, Cappa F, Moridis GJ. Modeling of fault activation and seismicity by injection directly into a fault zone associated with hydraulic fracturing of shale-gas reservoirs. *J Pet Sci Eng*. 2015;127:377–386.
38. Rutqvist J, Wu Y-S, Tsang C-F, Bodvarsson G. A modeling approach for analysis of coupled multiphase fluid flow, heat transfer, and deformation in fractured porous rock. *Int J Rock Mech Min Sci*. 2002;39(4):429–442.
39. Yuan Y, Xu T, Moore J, Lei H, Feng B. Coupled thermo–hydro–mechanical modeling of hydro-shearing stimulation in an enhanced geothermal system in the raft river geothermal field, USA. *Rock Mech Rock Eng*. 2020;53:5371–5388.
40. Lisjak A, Mahabadi O, Kaifosh P, Vietor T, Grasselli G. A preliminary evaluation of an enhanced FDEM code as a tool to simulate hydraulic fracturing in jointed rock masses. In: *ISRM EUROCK*. ISRM; 2014.
41. Grasselli G, Lisjak A, Mahabadi OK, Tatone BS. Influence of pre-existing discontinuities and bedding planes on hydraulic fracturing initiation. *Eur J Environ Civ Eng*. 2015;19(5):580–597.
42. Gischig VS, Preisig G. Hydro-fracturing versus hydro-shearing: a critical assessment of two distinct reservoir stimulation mechanisms. In: *ISRM Congress*. ISRM; 2015.
43. Watanabe N, Wang W, Taron J, Görke U, Kolditz O. Lower-dimensional interface elements with local enrichment: application to coupled hydro-mechanical problems in discretely fractured porous media. *Internat J Numer Methods Engrg*. 2012;90(8):1010–1034.

44. Rinaldi AP, Rutqvist J. Joint opening or hydroshearing? Analyzing a fracture zone stimulation at fenton hill. *Geothermics*. 2019;77:83–98.
45. Siebert P. *Laborversuche zur hydraulischen risserzeugung in dreiaxial belasteten granitquadern-grundlagen, versuchsentwicklung,-durchfuehrung und analyse* [Ph.D. thesis]. Dissertation, RWTH Aachen University, 2017; 2020.
46. Deb P, Salimzadeh S, Vogler D, Düber S, Clauser C, Settgast RR. Verification of coupled hydraulic fracturing simulators using laboratory-scale experiments. *Rock Mech Rock Eng*. 2021;54:2881–2902.
47. Clauser C, Willbrand K, Ziegler M, et al *Entwicklung eines Werkzeus zur Auslegung von HDR-Risssystemen*. RWTH Aachen University; 2015.
48. Permann CJ, Gaston DR, Andrš D, Carlsen RW, Kong F, Lindsay AD, et al MOOSE: Enabling massively parallel multiphysics simulation. *SoftwareX*. 2020;11:100430. http://dx.doi.org/10.1016/j.softx.2020.100430, URL http://www.sciencedirect.com/science/article/pii/S2352711019302973,
49. Wilkins A, Green CP, Ennis-King J. PorousFlow: a multiphysics simulation code for coupled problems in porous media. *J Open Source Softw*. 2020;5(55):2176. http://dx.doi.org/10.21105/joss.02176.
50. Krietsch H, Gischig VS, Doetsch J, et al Hydromechanical processes and their influence on the stimulation effected volume: observations from a decameter-scale hydraulic stimulation project. *Solid Earth*. 2020;11(5):1699–1729.
51. Min K-B, Rutqvist J, Tsang C-F, Jing L. Stress-dependent permeability of fractured rock masses: a numerical study. *Int J Rock Mech Min Sci*. 2004;41(7):1191–1210.
52. Lee H, Cho T. Hydraulic characteristics of rough fractures in linear flow under normal and shear load. *Rock Mech Rock Eng*. 2002;35(4):299–318.
53. Rutqvist J, Tsang C-F. Analysis of thermal–hydrologic–mechanical behavior near an emplacement drift at Yucca Mountain. *J Contam Hydrol*. 2003;62:637–652.
54. Giudicelli G, Lindsay A, Harbour L, et al 3.0 - MOOSE: Enabling massively parallel multiphysics simulations. *SoftwareX*. 2024;26:101690. http://dx.doi.org/10.1016/j.softx.2024.101690, URL https://www.sciencedirect.com/science/article/pii/S235271102400061X,
55. Rattez H, Stefanou I, Sulem J, Veveakis M, Poulet T. The importance of thermo-hydro-mechanical couplings and microstructure to strain localization in 3D continua with application to seismic faults. part II: Numerical implementation and post-bifurcation analysis. *J Mech Phys Solids*. 2018;115:1–29.
56. Rattez H, Stefanou I, Sulem J. The importance of thermo-hydro-mechanical couplings and microstructure to strain localization in 3D continua with application to seismic faults. part I: Theory and linear stability analysis. *J Mech Phys Solids*. 2018;115:54–76. http://dx.doi.org/10.1016/j.jmps.2018.03.004, URL https://www.sciencedirect.com/science/article/pii/S0022509617309626,
57. Platt JD, Rudnicki JW, Rice JR. Stability and localization of rapid shear in fluid-saturated fault gouge: 2. Localized zone width and strength evolution. *J Geophys Res Solid Earth*. 2014;119(5):4334–4359.
58. Stathas A, Stefanou I. Fault friction under thermal pressurization during large seismic-slip: Numerical analyses and extension of the model of frictional slip. *Int J Mech Sci*. 2023;248:108184.
59. Rutqvist J, Graupner B, Guglielmi Y, et al An international model comparison study of controlled fault activation experiments in argillaceous claystone at the mont terri laboratory. *Int J Rock Mech Min Sci*. 2020;136:104505.
60. Siebert P, Clauser C, Ziegler M. *Laborversuche zur hydraulischen risserzeugung in dreiaxial belasteten granitquadern-grundlagen, versuchsentwicklung,-durchführung und analyse*. Tech. rep. Lehrstuhl für Geotechnik im Bauwesen und Institut für Grundbau; 2017.
61. Selvadurai P, Selvadurai PA, Nejati M. A multi-phasic approach for estimating the Biot coefficient for grimsel granite. *Solid Earth*. 2019;10(6):2001–2014.